


## Introducing a lattice Boltzmann time-domain method: A thermodynamics-based approach for simulating quantum effects

Abed Zadehgol *Department of Mechanical Engineering, University of Tehran, Rezvanshahr 43841-119, Iran*

(Received 18 October 2021; accepted 5 January 2022; published 14 January 2022)

In this work, using the generalized Boltzmann equation of Zadehgol [*Phys. Rev. E* **94**, 023316 (2016)] a lattice Boltzmann time-domain (LBTD) method is proposed. The time-domain methods, such as the finite-difference time-domain method (FDTD), have been proposed by researchers, as tools in the study and design of semiconductor and optoelectronic devices. The LBTD inherits the main advantages of the lattice Boltzmann methods over the conventional methods, i.e., simplicity of the implementation, easy handling of complex geometries, and explicit algorithms which make the method highly suitable for efficient parallel processing. The theoretical findings have been verified by performing LBTD analysis on some benchmark structures.

DOI: [10.1103/PhysRevE.105.015307](https://doi.org/10.1103/PhysRevE.105.015307)

### I. INTRODUCTION

Time-domain methods are numerical techniques used for modeling computational electrodynamics and for studying quantum effects in electronic or optoelectronic devices. The methods are based on solutions of the time-dependent Schrodinger equation (TDSE), as in the finite-difference time-domain (FDTD) [1,2], finite element time-domain (FETD) [3], and spectral element time-domain (SETD) [4] methods, followed by a spectral analysis, to determine certain characteristics of the device, such as its eigen frequencies and eigenfunctions.

In the present work, a lattice Boltzmann time-domain (LBTD) method is introduced, in which the transient solution of the TDSE is provided by a kinetics-based method, using the generalized Boltzmann equation of Ref. [5]. The characteristics of the structure, next, are determined by performing a spectral analysis on the time-domain data.

The proposed quantum kinetic model inherits the main advantages of the lattice Boltzmann method (LBM) over the conventional methods, e.g., its simple algorithms for numerical implementations, easy and efficient procedures for defining the initial and boundary conditions, and local algorithms for efficient parallel programming.

Among other numerical methods which can be used to determine the quantum characteristics of the electronic devices governed by the TDSE, the exact diagonalization [6,7], and the imaginary time methods can be named.

The exact diagonalization method is used to extract exact information on finite systems. The exact results, however, can be obtained at a very high computational cost, due to the exponential growth of the Hilbert space dimension with the size of the quantum system [6]. The main limitation of this method is its restriction to small lattices, and thus properties in the thermodynamic limit are difficult to obtain [7].

In the imaginary time methods [2,8,9], the real time,  $t$ , is replaced by an imaginary time,  $it$ . This change of variable, also referred to as the Wick's rotation, converts the time-dependent Schrodinger equation into a diffusion type

equation using which certain spectral data, such as the eigen frequencies and eigenfunctions of the structure, can be extracted. Note that the ground state quickly dominates, as the system evolves in imaginary time [9], because its amplitude grows exponentially faster than the amplitudes of the other states. To detect the next eigen frequency and eigenstate, using the imaginary time method, therefore, one must remove the ground state from the initial state condition and repeat the simulation. Details of the removal procedure can be found in Refs. [2,9]. It is clear that to detect each eigen frequency and eigenstate, the simulation has to be repeated after performing a separate removal procedure, which add to the computational costs of the model.

Statistical mechanics has long been recognized as a valuable tool for connecting the micro and macro states to each other. It also provides a foundation using which the governing equations of the classical mechanics can be recovered, interpreted, justified, or understood. The recovery of the mass, momentum, and energy equations of the fluid dynamics from the Boltzmann equation are important examples of the application of the statistical mechanics in classical physics.

The formal analogies between Dirac and Boltzmann equations and between Schrödinger and Navier-Stokes equations, and the existence of connections between the heat and Schrodinger equation through replacement of the real time with an imaginary time, i.e., the so called Wick's rotation, have motivated researchers to propose quantum kinetic models. For example, fluid dynamics formulations of the Schrödinger and Dirac equations are proposed by researchers [10–12]. An interesting outlook on the lattice Boltzmann method and its applications in quantum mechanics and relativistic hydrodynamics can be found in Ref. [13].

Wigner and Moyal [14,15] proposed the following equation which is structurally similar to the classical Boltzmann equation:

$$\frac{\partial W}{\partial t} + \frac{p_\alpha}{m} \frac{\partial W}{\partial x_\alpha} = \Omega, \quad (1)$$

and it governs the evolution of the Wigner distribution function [14] as described below:

$$W = \frac{i}{\pi \hbar} \int \psi^*(x+y)\psi(x-y)e^{2ipy/\hbar} dy, \quad (2)$$

where  $x$  and  $y$  denote position, and  $p$  and  $\psi$  represent the momentum and wave function, respectively, and the ‘‘collision term,’’  $\Omega$ , is given by

$$\Omega = \frac{i}{2\pi \hbar^2} \int e^{-\frac{i}{\hbar}(p-p')\lambda} W(x, p') \xi(x, \lambda) d\lambda dp'. \quad (3)$$

Using a free parameter,  $\lambda$ , and denoting the potential by  $\Phi$ , the following relation is used to define  $\xi$ :

$$\xi(x, \lambda) = \left[ \Phi\left(x - \frac{\lambda}{2}\right) - \Phi\left(x + \frac{\lambda}{2}\right) \right]. \quad (4)$$

In the Wigner-Moyal equation, as described above, the collision term and relaxation time of the standard kinetic models are not explicitly identified. Taking advantage of the formal analogy between the collisionless Wigner and Boltzmann equations, however, Ref. [16] proposed a lattice kinetic method (also called the Lattice Wigner method) which can be used to solve the Wigner equation.

Numerical instabilities in Eq. (1) have been reported in Ref. [16], where it is mentioned that these instabilities can be reduced by inserting a regularizing artificial collision term, through selective numerical dissipation.

Using a kinetics-based approach and aiming to devise a generalized Boltzmann equation which can be used in transport of complex valued properties, Ref. [5] proposed the following generalized Boltzmann equation (GBE), in the scope of constant speed kinetic models [5,17–22]:

$$\frac{Df}{Dt} \equiv \left( \frac{\partial}{\partial t} + \nabla \right) f = -\frac{1}{\lambda} (f - f^{\text{eq}}), \quad (5)$$

where  $f = f_1 + if_2$ ,  $z = x_1 + ix_2$ ,  $t = t_1 + it_2$ ,  $v = v_1 + iv_2$ , and  $u = u_1 + iu_2$  are used to denote the complex valued probability density, position, time, and microscopic and macroscopic velocities of the fluid, respectively. Here,  $f^{\text{eq}}$  and  $\lambda$  are complex valued equilibrium distribution function (EDF) and relaxation time, respectively.

It is to be noted that, in contrast to the Wigner-Moyal equation, the collision term and the relaxation time of the GBE are identifiable, and there is no need to use an analogy to model these terms.

Defining the complex valued equilibrium probability density of:  $f^{\text{eq}} = \frac{\rho}{v-u}$ , and using the following relations:  $\rho = \int f dv = \int f^{\text{eq}} dv$  and  $\rho u = \int v f dv = \int v f^{\text{eq}} dv$ , to evaluate the density and velocity of the fluid, respectively, Ref. [5] shows that the GBE can recover the continuity and incompressible Navier Stokes equations, in the 2D-space, if the condition of purely real macroscopic fluid density can be enforce.

Defining the EDF by:  $f^{\text{eq}} = \frac{\psi}{2\pi}$  and using  $\psi = \int f d\theta$  for evaluating the wave function, in a separate study, Ref. [21] shows that the 2D Schrodinger equation can be recovered from the GBE, where the potential term is treated as a source term. This proof, however, is limited to the 2D space.

The paper has been organized as follows. In Sec. II, a mathematical formulation of the LBTd, which is not limited

to the 2D space, is proposed. In Sec. III details of the numerical implementation of the LBTd, are presented. In Sec. IV, numerical verification of the present method are presented. Finally, the paper is concluded in Sec. V.

## II. MATHEMATICAL FORMULATION

The constant speed kinetic model (CSKM), proposed in Refs. [5,17–22], is an entropic kinetic model obeying the non-conventional entropies of Burg and Tsallis. The fixed-speed particles with continuously varying direction of propagation reside on the surfaces of  $n$ -dimensional ( $n$ D) spheres which surround the computational nodes. Hence, the discretization of the velocity space, in the CSKM, is to be viewed as an implementation method, only, and not as a mathematical description.

Defining  $f^{\text{eq}} = \frac{\rho}{\sigma} v^{n-2} (v^2 - u^2) / (v^2 + u^2 - 2v_\alpha u_\alpha)^{n/2}$ , and employing  $\rho = \int f d\sigma$  and  $\rho u_\alpha = \int v_\alpha f d\sigma$ , in the  $n$ D space, Ref. [19] shows that the CSKM can recover the continuity and incompressible Navier Stokes equations. Here, the density and macroscopic velocity are denoted by  $\rho$  and  $u$ , respectively, and the area of the  $n$ D sphere surrounding the node is denoted by  $\sigma$ .

In the next section, it is shown that the GBE of Refs. [19,21] can recover the  $n$ D Schrodinger equation. This proof does not require a complex representation of the position and velocity vectors. Therefore, it is not limited to the two-dimensional space.

### A Chapman-Enskog analysis of the GBE

As shown in Ref. [21], the recovery of the Schrodinger equation from the GBE with an added complex valued source term,  $S$ , begins by expanding Eq. (5), using the method of Guo *et al.* [23] as follows:

$$f(\mathbf{x} + \mathbf{v}\delta t, \mathbf{v}, t + \delta t) - f(\mathbf{x}, \mathbf{v}, t) = -\frac{1}{\tau} [f(\mathbf{x}, \mathbf{v}, t) - f^{\text{eq}}(\mathbf{x}, \mathbf{v}, t)] + \left(1 - \frac{1}{2\tau}\right) \delta t S, \quad (6)$$

$$f^{\text{eq}}(\mathbf{x}, \mathbf{v}, t) = \psi(\mathbf{x}, \mathbf{v}, t)/m, \quad (7)$$

where the position and velocity vectors are denoted by  $\mathbf{x}$  and  $\mathbf{v} \in \{\mathbf{v}_1, \mathbf{v}_2, \mathbf{v}_3, \dots, \mathbf{v}_m\}$ , respectively, and the number of discrete velocities is depicted by  $m$ . Here,  $\mathbf{v}_k$  is the  $k$ th discrete velocity vector of the lattice structure.

The actual and equilibrium probability densities are denoted by  $f(\mathbf{x}, \mathbf{v}, t)$  and  $f^{\text{eq}}(\mathbf{x}, \mathbf{v}, t)$ , respectively. Note that  $f$  and  $f^{\text{eq}}$  are functions of the position and velocity vectors,  $\mathbf{x}$  and  $\mathbf{v}$ , respectively, and of the complex valued time,  $t$ . The position and velocity vectors can also be represented in tensor forms as:  $x_\alpha$  and  $v_\alpha$ , respectively.

In the upcoming discussions, to simplify the relations, the following abbreviations are used:

$$\delta t \equiv \delta \equiv \varepsilon, \quad (8)$$

$$\frac{\partial}{\partial t} \equiv \frac{\partial}{\partial t_0} + \delta \frac{\partial}{\partial t_1}, \quad (9)$$

$$A \equiv \left( \frac{\partial}{\partial t_0} + v_\alpha \frac{\partial}{\partial x_\alpha} \right), \quad (10)$$

$$B \equiv \frac{\partial}{\partial t_1}. \quad (11)$$

Following Ref. [24], the indexing parameter,  $\varepsilon$ , of the Chapman-Enskog (CE) expansion, is assumed to be of the same order of the time step,  $\delta t$  (also abbreviated by  $\delta$ ), as indicated by Eq. (8).

Using the “slow” and “fast” timescales,  $t_0$  and  $t_1$ , respectively, of the CE procedure, the probability density function,  $f$ , can be expanded as follows:

$$f = f^0 + \delta f^1 + \delta^2 f^2 + \delta^3 f^3 + \dots \quad (12)$$

A Taylor series expansion of  $f(\mathbf{x} + \mathbf{v}\delta t, \mathbf{v}, t + \delta t)$  around the point  $(\mathbf{x}, \mathbf{v}, t)$  of the phase space yields

$$\begin{aligned} f(\mathbf{x} + \mathbf{v}\delta t, \mathbf{v}, t + \delta t) &= f(\mathbf{x}, \mathbf{v}, t) + \delta t \left( \frac{\partial}{\partial t} + v_\alpha \frac{\partial}{\partial x_\alpha} \right) f(\mathbf{x}, \mathbf{v}, t) \\ &+ \frac{1}{2} (\delta t)^2 \left( \frac{\partial}{\partial t} + v_\alpha \frac{\partial}{\partial x_\alpha} \right)^2 f(\mathbf{x}, \mathbf{v}, t) + \dots \end{aligned} \quad (13)$$

Combining Eqs. (6) and (13), one obtains the following  $O(\delta^2)$  accurate relation:

$$\begin{aligned} \left[ \delta t \left( \frac{\partial}{\partial t} + v_\alpha \frac{\partial}{\partial x_\alpha} \right) + \frac{1}{2} (\delta t)^2 \left( \frac{\partial}{\partial t} + v_\alpha \frac{\partial}{\partial x_\alpha} \right)^2 \right] f \\ = -\frac{1}{\tau} [f(\mathbf{x}, \mathbf{v}, t) - f^0(\mathbf{x}, \mathbf{v}, t)] + \left( 1 - \frac{1}{2\tau} \right) \delta t S. \end{aligned} \quad (14)$$

Now, using the above relations and abbreviations, one arrives at the following result:

$$\begin{aligned} \left[ \delta(A + \delta B) + \frac{1}{2} \delta^2 (A + \delta B)^2 \right] (f^0 + \delta f^1 + \dots) \\ = -\frac{1}{\tau} (\delta f^1 + \delta^2 f^2 + \dots) + \left( 1 - \frac{1}{2\tau} \right) \delta t S, \end{aligned} \quad (15)$$

which yields the following  $O(\delta)$  order equation:

$$A f^0 = -\frac{1}{\tau} f^1 + \left( 1 - \frac{1}{2\tau} \right) S, \quad (16)$$

and the following  $O(\delta^2)$  order equation:

$$B f^0 + A f^1 + \frac{1}{2} A^2 f^0 = -\frac{1}{\tau} f^2. \quad (17)$$

Rewriting Eq. (16) as follows:

$$f^1 = \tau \left[ \left( 1 - \frac{1}{2\tau} \right) S - A f^0 \right], \quad (18)$$

and combining Eqs. (17) and (18), one obtains

$$B f^0 + \left( \frac{1}{2} - \tau \right) A^2 f^0 + \left( \tau - \frac{1}{2} \right) A S = -\frac{1}{\tau} f^2. \quad (19)$$

Using Ref. [23] for the  $nD$  CSKM [19], one can write

$$\psi = \int f^0 d\sigma = \int f d\sigma + \frac{1}{2} \delta t \int S d\sigma, \quad (20)$$

where  $d\sigma$  is the differential area of the  $nD$  sphere [19] surrounding a target node. Hence, one can write

$$\int (f - f^0) d\sigma = -\frac{1}{2} \delta t \int S d\sigma, \quad (21)$$

and, using Eq. (12), it can be simplified to obtain

$$\int f^1 d\sigma = -\frac{1}{2} \int S d\sigma. \quad (22)$$

Integrating Eq. (16) and using Eq. (22) to simplify the result, one can write

$$\frac{\partial \psi}{\partial t_0} = \int S d\sigma. \quad (23)$$

Note that  $f^0 = \psi/\sigma$ , for an elemental  $nD$  sphere with area of  $\sigma$ , surrounding the computational node. Hence, one can write:  $\int v_\alpha f^0 d\sigma = \frac{\psi}{\sigma} \int v_\alpha d\sigma = 0$ , due to the symmetric distribution of  $v_\alpha$  on the  $nD$  spatial directions.

Using the following complex valued source term:

$$S = -i\Phi f^0, \quad (24)$$

it can be shown that

$$\int A S d\sigma = \frac{\partial}{\partial t_0} \int S d\sigma. \quad (25)$$

Integrating Eq. (19), one obtains

$$\begin{aligned} \frac{\partial \psi}{\partial t_1} + \left( \frac{1}{2} - \tau \right) \int \left[ \frac{\partial^2}{\partial t_0^2} + v_\alpha v_\beta \frac{\partial}{\partial x_\alpha} \frac{\partial}{\partial x_\beta} + 2v_\alpha \frac{\partial}{\partial t_0} \frac{\partial}{\partial x_\alpha} \right] \\ \times f^0 d\sigma + \left( \tau - \frac{1}{2} \right) \frac{\partial}{\partial t_0} \int S d\sigma = 0. \end{aligned} \quad (26)$$

Note that the following relation holds:

$$\frac{\partial^2 \psi}{\partial t_0^2} = \frac{\partial}{\partial t_0} \left( \frac{\partial \psi}{\partial t_0} \right) = \frac{\partial}{\partial t_0} \int S d\sigma. \quad (27)$$

Inserting Eq. (27) into Eq. (26), one obtains

$$\frac{\partial \psi}{\partial t_1} + \left( \frac{1}{2} - \tau \right) \frac{\partial^2}{\partial x_\alpha \partial x_\beta} \int v_\alpha v_\beta f^0 d\sigma = 0. \quad (28)$$

For the symmetric velocities,  $v_\alpha$ , in the  $nD$  space, one can write  $\int v_\alpha v_\beta f^0 d\sigma = \int v_\alpha v_\beta \frac{\psi}{\sigma} d\sigma = \frac{\psi}{\sigma} \int v_\alpha v_\beta d\sigma = \frac{\psi}{\sigma} [v_0^2 \delta_{\alpha\beta}] \sigma$ , which yields

$$\int v_\alpha v_\beta f^0 d\sigma = \frac{v_0^2}{d} \psi \delta_{\alpha\beta}, \quad (29)$$

where  $d$  is the dimension of space,  $v_0$  is the magnitude of the microscopic velocity of the constant speed model, and  $\delta_{\alpha\beta}$  is Dirac's  $\delta$  function. Combining Eqs. (28) and (29), one can write

$$\frac{\partial \psi}{\partial t_1} + \frac{v_0^2}{d} \left( \frac{1}{2} - \tau \right) \frac{\partial^2 \psi}{\partial x_\alpha \partial x_\alpha} = 0. \quad (30)$$

Combining Eqs. (23) and (24), one can write

$$\frac{\partial \psi}{\partial t_0} = -i\Phi \psi. \quad (31)$$

Note that  $\frac{\partial \psi}{\partial t} = \frac{\partial \psi}{\partial t_0} + \delta \frac{\partial \psi}{\partial t_1}$ . Hence, combining Eqs. (30) and (31), one obtains

$$\frac{\partial \psi}{\partial t} + \frac{1}{2} \left( \frac{1}{2} - \tau \right) v_0^2 \delta t \nabla^2 \psi - \Phi \psi = 0. \quad (32)$$

Introducing a new term  $\kappa$  by setting  $\tau = \frac{1}{2} + i\kappa$ , one can recast Eq. (32) into the following form:

$$i \frac{\partial \psi}{\partial t} + \left( \frac{1}{2} v_0^2 \kappa \delta t \right) \nabla^2 \psi - \Phi \psi = 0, \quad (33)$$

which, defining  $\alpha = -\frac{1}{2} v_0^2 \kappa \delta t$ , can be rewritten in the following canonical form:

$$i \frac{\partial \psi}{\partial t} + \alpha \nabla^2 \psi + \Phi \psi = 0. \quad (34)$$

Hence, the complex valued relaxation time,  $\tau$ , and the source term,  $S = -i\Phi f^{\text{eq}}$ , of the GBE, can be used to adjust the coefficient of Laplacian,  $\alpha$ , and the potential term,  $\Phi$ , of the recovered time-dependent Schrödinger equation. The efficiency and accuracy of the method is rigorously investigated and verified by simulating some example problems, in Sec. IV.

### III. NUMERICAL IMPLEMENTATIONS

Despite the relative complexity of the derivations of Sec. II, the implementation of the LBTB is simple. In this section, the numerical method is summarized, and some notes and clarifications are presented.

#### A. Summary of the implementation procedure

As the first step, the probability densities denoted by  $f_k$ , for direction of  $k \in \{1, 2, 3, 4, 5, 6\}$  and at all locations denoted by the position vector of  $\mathbf{r}$ , are initialized, using  $f_k(\mathbf{r}, 0) = f_k^{\text{eq}}$ , where  $f_k^{\text{eq}} = \frac{1}{6} \psi(\mathbf{r}, 0)$  is the equilibrium probability density given by Eq. (7) with  $m = 6$  for the six velocity hexagonal and orthogonal lattices of the present work. The initial value of  $\psi(\mathbf{r}, 0)$  depends on the problem at hand, and it is known at the beginning of each simulation.

The collision stage, in the present work, consists of the following steps: (i) Evaluating the local values of the wave function using the method of Ref. [23] and as described in Sec. III D,  $\psi(\mathbf{r}, t) = \sum f_k^{\text{eq}}(\mathbf{r}, t) = \sum f_k(\mathbf{r}, t) + \frac{1}{2} \delta t \sum S_k$ , which, using  $S_k = -i\Phi f_k^{\text{eq}}$ , can be simplified to obtain  $\psi(\mathbf{r}, t) = \sum f_k(\mathbf{r}, t) / (1 + \frac{1}{2} i\Phi)$ ; (ii) evaluating the equilibrium probability densities using  $f_k^{\text{eq}}(\mathbf{r}, t) = \frac{1}{6} \psi(\mathbf{r}, t)$ ; (iii) relaxing the probability densities,  $f_k$ , toward  $f_k^{\text{eq}}$ , to evaluate the post collision probability densities,  $\tilde{f}_k = f_k - (f_k - f_k^{\text{eq}}) / \tau$ , where the relaxation time can be set to control the coefficient of the Laplacian term of the Schrödinger equation.

In the streaming stage, the outgoing probabilities,  $\tilde{f}_k$ , are streamed on the links of a regular lattice to update the values of the probability densities of their neighboring nodes. Note that the bounce-back boundary condition of the conventional LBM has been used to model the infinite wall potential, in the present simulations.

Based on the above description, the implementation of the present model is similar to that of the conventional lattice Boltzmann models, and the only differences are the use of complex valued probability densities and a new definition of the equilibrium probability density function in the proposed model.

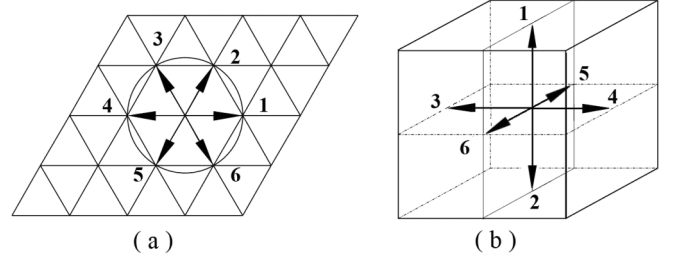


FIG. 1. Hexagonal (a) and orthogonal (b) six velocity lattices for the present 2D and 3D simulations.

#### B. Notes on complex valued properties

It is to be noted that, in the present kinetic model, the conventional algebra of real variable and functions is replaced by the algebra of complex valued quantities and functions. The “complex valued probability” of the generalized model can be viewed as the perturbations of the complex valued equilibrium distribution function, for which a precise definition is provided. Moreover, the perturbations are governed by the generalized Boltzmann equation (GBE). An attempt to draw analogies between the conventional and complex valued probabilities, thus, is not necessary, while it can be misleading.

The following clarification regarding the “collision” and “streaming” stages of the GBE are presented. The collision stage, by definition, is the stage during which the complex valued probabilities are updated, and the streaming stage is governed by a pure advection equation, using which the updated “probabilities” are streamed on the links of a regular lattice.

#### C. Lattices and units

Figure 1(a) shows a hexagonal lattice [17–19,21,22], in which the height-to-width ratio of a unit cell is equal to  $\frac{\sqrt{3}}{2} \approx 0.86$ . For a square domain, the same column-to-row ratio should be respected. Hence,  $G_n$  is defined as a hexagonal lattice with dimensions of  $n \times 43$  columns and  $n \times 50$  rows. In this work, the  $G_2$ ,  $G_3$ , and  $G_4$  lattices have been used, in Sec. IV. The discrete velocities,  $\mathbf{v}_k = (v_{kx}, v_{ky})$ , are defined by:  $v_{kx} = v \cos[\frac{(k-1)\pi}{3}]$  and  $v_{ky} = v \sin[\frac{(k-1)\pi}{3}]$  for  $k \in \{1, 2, 3, 4, 5, 6\}$ .

For the 3D simulations of this work, the orthogonal lattice shown in Fig. 1(b) is used, where the discrete velocities, of the model are given by:  $\mathbf{v}_{1-2} = (\pm 1, 0, 0)$ ,  $\mathbf{v}_{3-4} = (0, \pm 1, 0)$ , and  $\mathbf{v}_{5-6} = (0, 0, \pm 1)$ .

The unit of length in the lattice Boltzmann models is the distance from each node to a neighboring node, and the unit of time (also referred to as one time step or as one iteration) is the time required for a virtual particle to travel from one node to a neighboring node. In the following subsections, the technical details of the LBTB method are presented.

#### D. Updating $\psi$ using the method of Ref. [23]

Following the method of Guo *et al.* [23] and using Eq. (20), one can write  $\psi = \int f d\sigma + \frac{1}{2} \delta t (-i\Phi \psi)$ , which yields the

following result:

$$\psi = \frac{1}{1 + \frac{1}{2}i\Phi\delta t} \int f d\sigma. \quad (35)$$

In this work, Eq. (35) has been used, after each update of the probability density function,  $f$ , to evaluate the wave function at the computational nodes.

Note that, in lattice units  $\delta t = 1$ , which leads to further simplification of Eq. (35).

### E. Imposing initial and boundary conditions

Knowing the initial states,  $\psi$ , the probability density function,  $f$ , can be initialized, as follows. Using Eq. (7) and for the six velocity lattices, the following relation is used:  $f(\mathbf{x}, \mathbf{v}, 0) = f^{\text{eq}}(\mathbf{x}, \mathbf{v}, 0) = \frac{1}{6}\psi(\mathbf{x}, 0)$ , to initialize the probability densities. To impose a Dirichlet boundary condition of  $\psi(\mathbf{x}, t) = \psi_0$ , the probability density is set equal to the equilibrium density which corresponds to  $\psi_0$ , using:  $f(\mathbf{x}, \mathbf{v}, t) = \frac{1}{6}\psi_0$ . The potential term,  $\Phi$ , can be adjusted by setting the source term  $S_k = -i\Phi f_k^{\text{eq}}$ , as mentioned in Sec. II A.

It should be noted that the ‘‘bounce-back boundary condition’’ of the lattice Boltzmann method can be used to impose the infinite wall boundary condition, instead of using the source term and employing large values of potential,  $\Phi$ . The advantage of the bounce-back model is that it preserves the total probability, and saves the need for a normalization procedure. Recall that, due to the quantum tunneling effect, a complete isolation of the structure is not possible, and there will always be a diffusion of ‘‘probable states,’’ even if large potentials are employed to isolate the structure.

Finally, the perfectly matched layer (PML) absorbing boundary condition, in time-domain methods, has been proposed and successfully implemented [25,26], to reduce noisy reflection of the wave function from the boundaries. In the lattice Boltzmann method, the PML has also been implemented to reduce noisy reflections of acoustic waves [27]. Hence, a similar approach can possibly be used in the proposed LBTD method. A comprehensive and detailed study on this matter is beyond the scope of this work, while it is suggested as a future work.

### F. Data sampling and analysis in the time and frequency domains

The solution of the Schrodinger equation can be split into time and space-dependent functions [1]:

$$\psi(\mathbf{x}, t) = \sum_{n=1}^N c_n e^{-i\omega_n t} \xi_n(\mathbf{x}). \quad (36)$$

Hence, probing the  $\psi$  field at a given point of  $\mathbf{x} = \mathbf{x}_0$ , yields the following time-dependent function:

$$A(t) = \psi(\mathbf{x}_0, t) = \sum_{n=1}^N c_n e^{-i\omega_n t} \xi_n(\mathbf{x}_0), \quad (37)$$

which can be used in the subsequent frequency analysis. The choice of the probing point(s) and a preprocessing of the time-domain data, as suggested by some researchers (e.g., Refs. [1,9]), can help improve the results.

### 1. Collecting and assembling the time-domain data

As mentioned in Ref. [9], to obtain a suitable time-domain data, the entire computational domain can be used to generate the desired time-dependent signal.

Using the linear property of the time-dependent Schrodinger equation, the temporal data is prepared, as follows: (i) after each time step and for all nodes  $i$  and  $j$  of the computational domain, the corresponding values of the wave function,  $\psi(i, j, t)$  are stored; (ii) to each node of the computational domain a unique random number  $-\frac{1}{2} \leq w(i, j) \leq \frac{1}{2}$  is assigned; (iii) the time-domain signal is now defined as the following linear combination of the collected data:

$$B(t) = \sum_{i=1}^M \sum_{j=1}^N w(i, j) \psi(i, j, t). \quad (38)$$

The time-domain data, in the present work, is obtained using the above mentioned procedure of Ref. [9], and it has been used in the subsequent spectral analysis, as described in Sec. IV.

### 2. Determining the eigenfrequencies and eigenstates using forward and inverse Fourier transforms

The standard procedure, in time-domain methods, include a numerical solution of the time-dependent Schrodinger equation followed by a spectral analysis of the temporal data [1], to detect the eigen frequencies of the device under study. The corresponding eigenstates, next, are determined by performing an online inverse Fourier transform of the frequency data. To reduce the computational costs, fast Fourier transforms can be used, if precisely  $2^N$  samples are collected [1].

### 3. The Hanning window method

Discontinuities in the time-domain signal result are sources of errors which often appear as false noises in the frequency domain (i.e., in the Fourier transform of the temporal signal). The two obvious discontinuities of the time-domain data occur at the beginning and at the end of the simulation. The time-domain signal can be improved using a weighting function,  $w(t)$ , which reduces the significance of data collected at the initial and final stages of the simulation.

The Hanning window procedure, with a weighting function of:  $w(t) = \frac{1}{2}[1 - \cos(2\pi t)]$ , has been used in the present simulations. Here,  $t = i/T$  is a rescaled time,  $i$  denotes the current time step, and  $T = \text{Max}(i) = 2^N$  is the number of samples. As mentioned in Sec. III F 1, the number of data samples should be  $2^N$ , so that the fast Fourier transform (FFT) method can be used in place of the standard Fourier transform. The rescaled temporal signal can be rewritten as:  $\tilde{\psi}(\mathbf{x}, t) = w(t)\psi(\mathbf{x}, t)$ .

### 4. A recursive signal filtration (RSF)

The test signal should contain the eigenfrequencies which are to be detected, since the Fourier transform can only reveal the eigenfrequencies which are present in the given test signal (state). Therefore, a white noise, i.e., a random collection of quantum states, is the best choice for acquiring information on the eigenstates of an unknown structure. However, a white noise is also more prone to excessive noise than an orderly test

signal, such as the stationary and coherent states of examples 1 and 2 (Secs. IV A and IV B). Using the LBTB method, it is shown that a white noise can be used to detect the eigen frequencies and evaluate the eigenstates of an unknown structure. In the present work, a recursive signal filtration (RSF) method is proposed, to verify and improve the accuracy of the computed eigenstate. The RSF procedure can be summarized as follows:

Using the standard procedure, as mentioned in Ref. [1], a random state (a white noise) is used as the initial condition and a Fourier analysis is performed to detect the eigen frequencies. The simulation is repeated, at one of the eigenfrequencies, while an online inverse Fourier transform is performed, to construct a secondary state.

In the previous works, it is assumed that the secondary state is an eigenstate, while, in this work, the RSF comes into play by introducing a verification and a correction procedure, as follows:

Using Born's interpretation of the wave function, the probability of finding a particle at  $(\mathbf{x}, t)$  is given by:  $\rho(\mathbf{x}, t) \equiv \psi(\mathbf{x}, t) \overline{\psi}(\mathbf{x}, t)$ . The verification now begins with repeating the simulation using the secondary state as the initial condition, while another online inverse Fourier transform is performed to construct a tertiary state.

If the secondary state is an eigenstate, then it is an stationary state; and the following term which measures deviations from being stationary is evaluated:

$$\text{err}(t) = \frac{\sum_i \sum_j |\rho_{i,j}^t - \rho_{i,j}^0|}{\sum_i \sum_j |\rho_{i,j}^0|}, \quad (39)$$

where the probability densities denoted by  $\rho_{i,j}^t$  and  $\rho_{i,j}^0$  pertain to the current and initial states, respectively. If the error term is negligible, then the secondary state is indeed an eigenstate, or else, if the error is not negligible, then the simulation is repeated, using the tertiary state as the initial condition, and the above verification and correction steps are repeated.

Based on the results of this work, one or two iterations of the RSF can greatly enhance the results, as shown in Fig. 11 of example 4 (Sec IV D).

#### IV. RESULTS AND DISCUSSIONS

The results reported in this section are obtained by performing numerical simulations, using a home-made C program and on a CPU with the following specifications: Processor: Intel Core i7-7500U CPU @ 2.70 GHz and 2.90 GHz with installed memory (RAM) of 16.0 GB.

The accuracy and efficiency of the proposed LBTB, in the present section, has throughly been investigated. The well known benchmark problems of two- and three-dimensional (2D and 3D) harmonic oscillators (HO), for which analytical solutions are available, are simulated. In addition to the above, a modification of the 2D HO has been simulated, by adding a circular infinite wall to the standard problem.

In this analysis, the following steps are taken: (i) the initial condition is set using either a stationary state, or a coherent state (generated by slightly dislocating an existing stationary state), or a random state (a white noise), (ii) the standard procedure of detecting the eigen frequencies and construct-

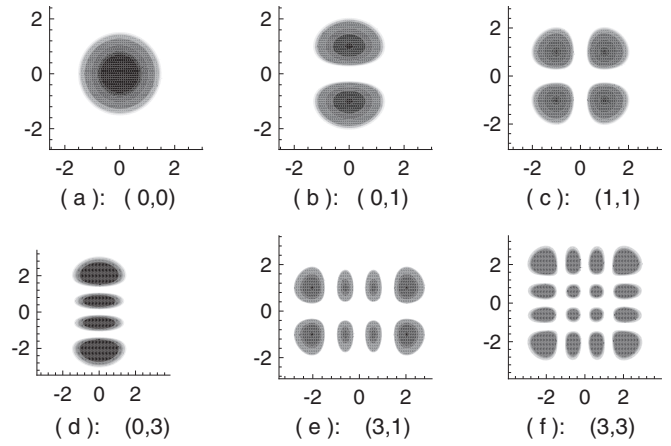


FIG. 2. The probability density contours, calculated using Eq. (43), for various quantum numbers of  $p$  and  $q$  in Eq. (42).

ing the eigenstates are followed, using a Fourier transform of the time-domain data and another online inverse Fourier transform of the frequency data, and, finally, (iii) a recursive signal filtration (RSF) procedure is introduced and used to verify and correct the computed eigenstates. (iv) the lattice size and the simulation time (in minutes) are reported, for each of the following examples, so that the computational costs of the proposed model can be estimated.

##### A. Example 1: Stationary states as initial condition

The quantum harmonic oscillator is an important benchmark problem, since its exact solutions are known. For the one-dimensional harmonic oscillator (1D HO) with potential of  $\phi(x) = \frac{1}{2}m\omega^2 x^2$ , one particular class of stationary states is given by

$$\psi_n(x) = \frac{1}{\sqrt{2^n n!}} \left( \frac{m\omega}{\pi \hbar} \right)^{1/4} e^{-\frac{m\omega x^2}{2\hbar}} H_n \left( \sqrt{\frac{m\omega}{\hbar}} x \right), \quad (40)$$

where  $H_n(x)$  is the Hermite polynomial of rank  $n$ , and  $m$  and  $\omega$  represent the mass and angular frequency of the wave packet, respectively. Moreover, to simplify the relations, Planck units are adopted, i.e.,  $\hbar$  is set equal to unity. It can be shown that, for the 2D harmonic oscillator (2D HO) with potential of

$$\phi(x, y) = \frac{1}{2}m\omega^2(x^2 + y^2), \quad (41)$$

stationary solutions of the following form exists:

$$\psi_{p,q}(x, y) = \psi_p(x)\psi_q(y). \quad (42)$$

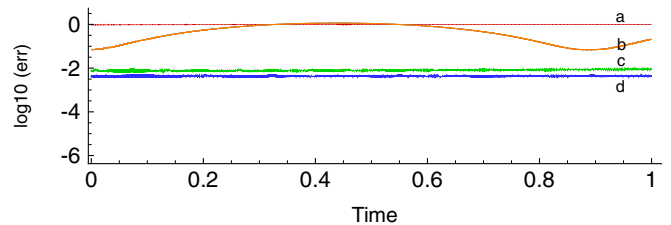


FIG. 3. A grid study and error analysis for various lattice sizes and for quantum numbers of  $p = 0$  and  $q = 3$ .

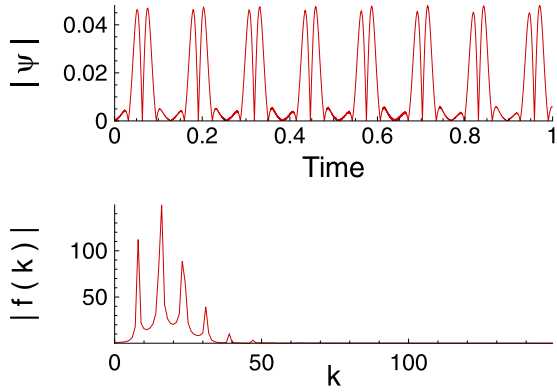


FIG. 4. The time-domain data (top) and its fast Fourier transform (bottom) for example 2.

For a square domain defined by:  $-5 \leq x, y \leq +5$ , the simulation is performed on hexagonal lattices  $G_2$ ,  $G_3$ , and  $G_4$ , and the stationary solution given by Eq. (42) with  $m = 1$  and  $\omega = 1$  is imposed as the initial condition. For the spectral analysis a total of  $2^{15}$  data points have been collected. Using the hexagonal lattice,  $G_4$ , with  $173 \times 200$  nodes and for a total of 32 768 iteration the execution time was 3 min on the machine specified in Sec. IV.

According to Born's interpretation [28] of the wave function, the probability density of finding a particle at a given location and time,  $\rho$ , is given by

$$\rho = \psi_1^2 + \psi_2^2. \tag{43}$$

Figure 2, for various quantum numbers of  $(p, q)$ , shows the contour plots of the probability density,  $\rho$ . Additionally, using Eq. (39), deviations of the probability densities from the initial state can be evaluated. The results are shown in Fig. 3, where the logarithm (in base 10) of the error, has been plotted versus time. The results obtained for the the  $G_2$ ,  $G_3$ , and  $G_4$  lattices are denoted by  $b$ ,  $c$ , and  $d$ . Using the  $G_3$  lattice, a white noise initial condition, has also been simulated and the result, denoted by  $a$  in the same figure, can be used as a basis of comparison. As expected, for an stationary state the variations of the probability densities,  $\rho$ , versus time is negligible.

**B. Example 2: Coherent states as initial condition**

In the second example, the 2D domain is defined by  $-5 \leq x, y \leq +5$ , and the lattice Boltzmann simulation is performed on the  $G_3$  lattice of Sec. III E.

Using the hexagonal lattice,  $G_3$ , with  $129 \times 150$  nodes and for a total of 32 768 iteration the execution time was 2 min on the machine specified in Sec. IV.

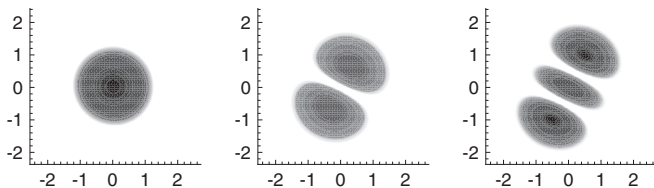


FIG. 5. The probability density contours, calculated using Eq. (43), for the first three eigenstates of example 2.

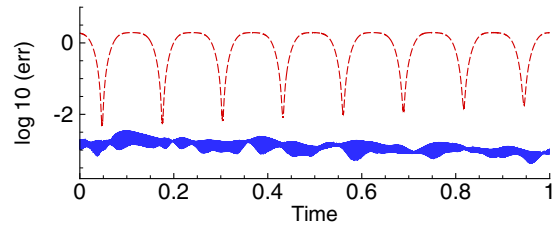


FIG. 6. Deviations from stationary state in example 2.

The initial condition, for the wave function, is given by Eq. (42) with a shifted  $x$  and  $y$  coordinates of  $x \rightarrow x + 0.5$  and  $y \rightarrow y + 1.5$ , respectively, and with the following settings:  $m = 1$ ,  $\omega = 2$ , and  $(p, q) = (0, 0)$ .

The potential function is defined by Eq. (41), inside the box, while the bounce-back boundary condition of the conventional lattice Boltzmann method is imposed at the boundaries to model an infinite potential at the faces of the cube. Additionally,  $\psi = 0.0 + 0.0i$  is imposed, as a Dirichlet condition, on the boundaries. Based on the simulation results, and as expected, the influence of the boundary condition on the results is related to the strength of the potential field.

Figure 4 shows the magnitudes of the time-domain data (top) and its Fourier transform (bottom) in the frequency domain. The time-domain data has been collected, at a point  $\mathbf{P}$  in the computational domain, and the Fourier transform of the time-dependent signal is given by

$$f(k) = \int_{-\infty}^{+\infty} \psi(\mathbf{p}, t) e^{-2\pi i k t} dt, \tag{44}$$

As shown in Fig. 4 (bottom), the first four peaks in the transformed (frequency domain) signal occur at  $k = 8, 16, 23, 31$ . The corresponding eigenstates can be constructed by following the procedures of Sec. III.

Figure 5, shows the contour plots of the probability density,  $\rho$ , for the first three detected eigen frequencies which occur at  $k = 8, 16, 23$ .

Using Eq. (39), deviations of the probability densities from their initial values, are evaluated, and the result is shown, in Fig. 6 (top). The oscillations of the error are due to the fact that the initial coherent state resembles a classical harmonic oscillator which periodically returns to its initial state.

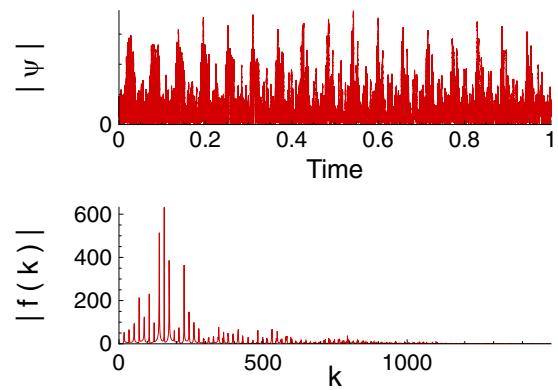


FIG. 7. The time-domain data (top) and its fast Fourier transform (bottom) for example 3.

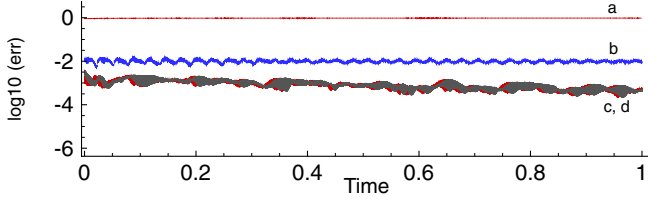


FIG. 8. Deviations from stationary state in example 3.

Figure 6 (bottom), using the RSF procedure of Sec. III F 4, shows that the computed eigenstate corresponding to  $k = 23$  is indeed a stationary state for which the deviations of probability density can be neglected with a second-order accuracy.

**C. Example 3: White noise initial condition**

In the third numerical test, a white noise (a random state) is used as the initial condition. The time-domain signal is collected using the procedure of Sec. III F 1, and the same procedures of the previous sections are followed to obtain the eigen frequencies and eigenstates.

Using the hexagonal lattice, G4, with  $173 \times 200$  nodes and for a total of 32 768 iteration the execution time was 3.5 min on the machine specified in Sec. IV.

The magnitude wave function is shown in Fig. 7 (top), and the magnitude of its Fourier transform is shown in Fig. 7 (bottom). Moreover, results of the RSF procedure, shown in Fig. 8 (bottom), clearly indicate that the secondary state is indeed a stationary state.

Note that the initial state is a random state, yet an axis of symmetry can be observed in the contour plots of the probability densities, as shown in Fig. 9. Appearance of such symmetries, for a random initial state and under a perfectly symmetric boundary condition (for example, using a circular wall or employing a strong potential field which does not allow significant interactions with wall), can be the subject of additional studies, as it may reveal useful information on the dynamics of the quantum states governed by the time-dependent Schrodinger equation.

**D. Example 4: A modified 2D HO with inner wall**

In the fourth example, the standard 2D HO is modified by placing an infinite wall of circular shape and centered at the origin. In the space between the inner wall and the outer boundaries, a random distribution of the wave function (white noise) is used, as the initial condition.

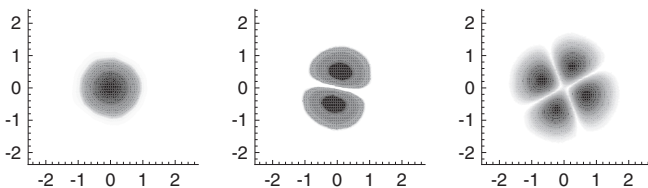


FIG. 9. The probability density contours, calculated using Eq. (43), for the first three eigenstates of example 3.

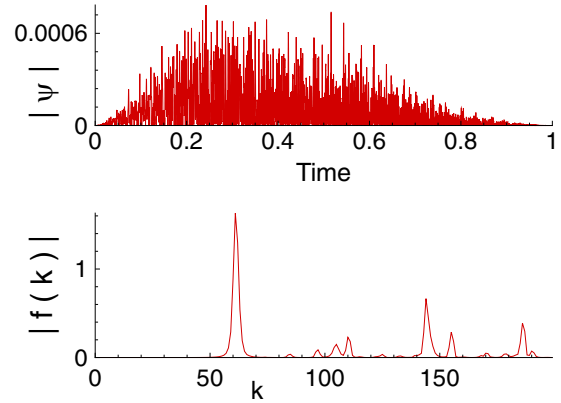


FIG. 10. The time-domain data (top) and its fast Fourier transform (bottom), in example 4.

Using the hexagonal lattice, G3, with  $129 \times 150$  nodes and for a total of 32 768 iteration the execution time was 2.2 min on the machine specified in Sec. IV.

In this example, the “bounce-back” and a Dirichlet boundary condition of  $\psi = 0 + 0i$  have been imposed at the inner and outer boundaries of the domain. It should be noted that the “bounce-back” boundary condition, can be used to model an ideal infinite wall, in the sense that the bounce-back model does not allow a passing of information through the wall, and the system under study can be fully isolated. As shown in Fig. 10 (top), the time-domain signal has a larger amplitude in the middle than in the ends. This is because the Hanning window method of Sec. III F 3 is used to reduce the noise due to discontinuities in the initial and final portions of the signal.

Figure 10 (bottom), shows that the first three peaks in the magnitude of the transformed (frequency domain) signal occur at  $k = 61, 144, 155$ . Using the procedures of Sec. III, the eigenstates corresponding to  $k = 144$  is constructed, and the result of the RSF iterations are shown in Fig. 11. The deviations of the probability density,  $\rho$ , from its initial value,  $\rho_0$ , for the eigenstate corresponding to  $k = 144$ , are shown in Fig. 12.

**E. Example 5: 3D harmonic oscillator**

In the fifth and final example, the present model is used to simulate a 3D quantum harmonic oscillator bounded by a cubical box with  $-2.5 \leq x, y, z \leq +2.5$ .

Using an orthogonal lattice of size  $70 \times 70 \times 70$ , and for a total of 32 768 iteration the execution time was 71 min on the machine specified in Sec. IV.

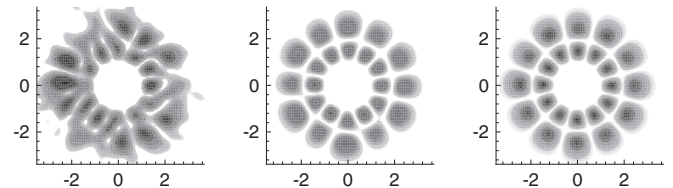


FIG. 11. The probability densities obtained for the modified 2D HO potential with inner wall.



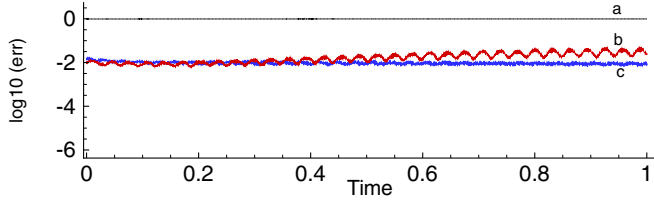


FIG. 12. Deviations from stationary state in example 4.

It can be shown that, for the 3D harmonic oscillator (3D HO) with potential of

$$\phi(x, y, z) = \frac{1}{2}m\omega^2(x^2 + y^2 + z^2), \quad (45)$$

stationary solutions of the following form exists:

$$\psi_{p,q,s}(x, y, z) = \psi_p(x) \psi_q(y) \psi_s(z), \quad (46)$$

where  $\psi_\gamma(\xi)$  is a stationary solution of the 1D harmonic oscillator, given by Eq. (40).

The initial condition for the wave function is given by Eq. (46) with a shifted  $x$  coordinate of  $x \mapsto x + 0.25$  and with the following parameter settings:  $m = 1$ ,  $\omega = 2$ , and  $p = q = s = 0$ . The potential function is defined by Eq. (45), inside the box, while the bounce-back boundary condition of the conventional lattice Boltzmann method is imposed at the boundaries to model an infinite potential at the faces of the cube. Additionally, a Dirichlet condition of  $\psi = 0.0 + 0.0i$  is imposed on the boundaries.

For the spectral analysis, a total of  $2^{15}$  data points have been collected following the procedure of Sec. III F. The bell shape of temporal signal is due to the application of the Hanning window method described in Sec. III F 3. The magnitude of the complex valued temporal signal is shown in Fig. 13 (top).

Next, the Fourier transform of the time-domain data is obtained. The magnitude of the transformed signal in the frequency domain is shown in Fig. 13 (bottom), using which the first four detected eigen frequencies occur at  $k = 35, 83, 130, 178$ . Following the procedure of Sec. III F 2, the corresponding eigenstates are computed.

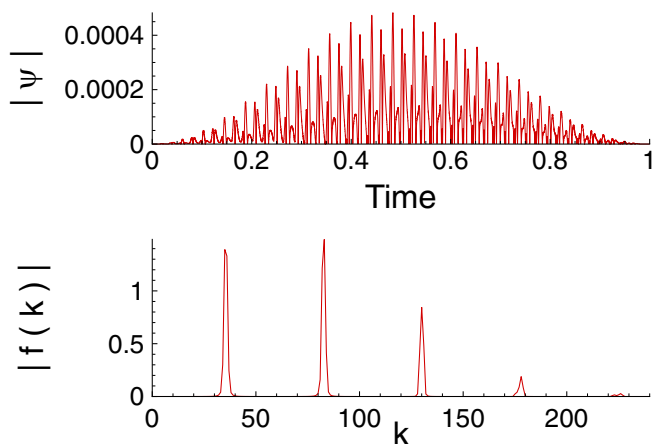


FIG. 13. The time-domain data (top) and its fast Fourier transform (bottom) for example 5.

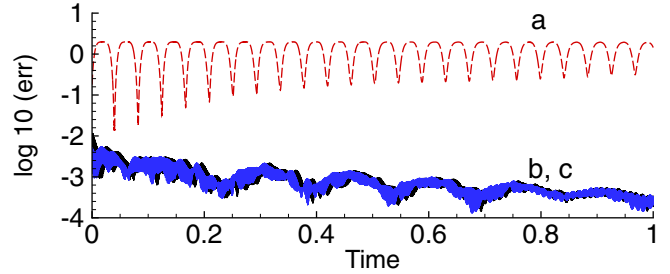


FIG. 14. Deviations from stationary state in example 5.

Using Eq. (39) and repeating the same procedures of example 2, deviations of the probability densities from their initial values, are evaluated, and the result is shown in Fig. 14 (top). The oscillations of the error, denoted by Fig. 14(a), are due to the fact that the initial coherent state resembles a classical harmonic oscillator which periodically returns to its initial state. Next, using the RSF procedure of Sec. III F 4, the accuracy of the eigenstate corresponding to  $k = 83$  is checked. The results of the first and second RSF iterations are denoted by Figs. 14(b) and 14(c), respectively.

In Fig. 15, for the first four detected eigenstates, the contour plots of the probability density (referred to as orbitals, hereafter) are shown, in which the orbitals are symmetrically distributed about the  $x$  axis.

Recall that the initial condition is imposed by shifting the  $x$  coordinates in Eq. (46) according to  $x \mapsto x + 0.25$ . In other words, the initial condition has been enforced by dislocating an existing stationary solution along the  $x$  axis. Using the existing symmetries, a dislocation of  $y \mapsto y + 0.25$  yields a degenerate state whose axis of symmetry is aligned with the  $y$  axis.

The eigen frequencies and eigenstates can optimally be detected if the initial state is chosen to be a random state which is a superposition of a large number of eigenstates. To detect all eigenstates of the structure, however, one may need to repeat the simulation with different initial conditions, as shown in this work and as reported by others [2]. Additionally, the issue of noises which are the sources of false results in the spectral analysis, have been addressed by researchers, and, as a partial remedy, the removal of excessive noise using

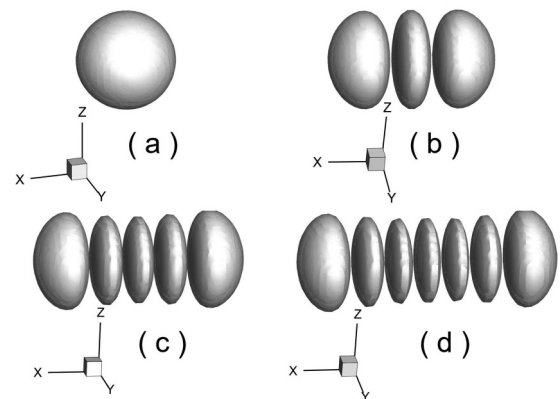


FIG. 15. 3D contour plot of the probability densities for the 3D harmonic oscillator of example 5.

filtration procedure, such as the Hanning window method [1] or the RSF procedure of the present work, have been suggested.

## V. CONCLUSION

In the present work, using the generalized Boltzmann equation (GBE) of Zadehgol [5] and Zadehgol and Khazaeli [22], a lattice Boltzmann time-domain method is proposed, in which the collision term and the relaxation time of the GBE model can be identified and are not constructed on the basis of an analogy.

It is shown that methods of implementation of the boundary conditions and source terms of the LBM (with real valued properties) can directly be applied to the present model (with complex valued properties). The present model, additionally,

inherits the main features of the LBM, such as (i) simple algorithms, (ii) easy handling of complex geometries, and (iii) being suitable for parallel processing. Hence, from the computational standpoint, it provides an efficient tool for the quantum mechanic simulations and studies, using the existing tools of the computational fluid dynamics (CFD).

Using the Chapman-Enskog analysis, it is shown that the Schrodinger equation is a second-order approximation of the GBE. Higher-order approximations of the GBE, thus, may provide more details and information. Further study on this matter is suggested.

## ACKNOWLEDGMENT

This work was supported by the Iran National Science Foundation (INSF) (Grant No. 99002455).

- 
- [1] D. M. Sullivan, *Quantum Mechanics for Electrical Engineers* (John Wiley & Sons, New York, 2012).
  - [2] I. W. Sudiarta and D. W. Geldart, *J. Phys. A: Math. Theor.* **40**, 1885 (2007).
  - [3] H. Gotoh, M. Koshiba, and Y. Tsuji, *IEICE Electron. Express* **8**, 1361 (2011).
  - [4] C. Cheng, Q. H. Liu, J.-H. Lee, and H. Z. Massoud, *J. Comput. Electron.* **3**, 417 (2004).
  - [5] A. Zadehgol, *Phys. Rev. E* **94**, 023316 (2016).
  - [6] A. Weiße and H. Fehske, in *Computational Many-Particle Physics* (Springer, Berlin, 2008), pp. 529–544.
  - [7] H. Lin, J. Gubernatis, H. Gould, and J. Tobochnik, *Comput. Phys.* **7**, 400 (1993).
  - [8] P. Bader, S. Blanes, and F. Casas, *J. Chem. Phys.* **139**, 124117 (2013).
  - [9] N. Bigaouette, E. Ackad, and L. Ramunno, *Comput. Phys. Commun.* **183**, 38 (2012).
  - [10] S. Succi and R. Benzi, *Physica D* **69**, 327 (1993).
  - [11] S. Succi, *Phys. Rev. E* **53**, 1969 (1996).
  - [12] S. Succi, F. Fillion-Gourdeau, and S. Palpacelli, *EPJ Quant. Technol.* **2**, 12 (2015).
  - [13] S. Succi, *Europhys. Lett.* **109**, 50001 (2015).
  - [14] E. Wigner, *Phys. Rev.* **40**, 749 (1932).
  - [15] J. E. Moyal, *Math. Proc. Camb. Phil. Soc.* **45**, 99 (1949).
  - [16] S. Solorzano, M. Mendoza, S. Succi, and H. J. Herrmann, *Phys. Rev. E* **97**, 013308 (2018).
  - [17] A. Zadehgol and M. Ashrafizaadeh, *J. Comput. Phys.* **274**, 803 (2014).
  - [18] A. Zadehgol, M. Ashrafizaadeh, and S. Musavi, *Comput. Fluids* **105**, 58 (2014).
  - [19] A. Zadehgol, *Phys. Rev. E* **91**, 063311 (2015).
  - [20] A. Zadehgol and M. Ashrafizaadeh, *Int. J. Mod. Phys. C* **27**, 1650088 (2016).
  - [21] A. Zadehgol and R. Khazaeli, *Phys. Rev. E* **98**, 053307 (2018).
  - [22] A. Zadehgol, *Int. J. Mod. Phys. C*, 2250025 (2021).
  - [23] Z. Guo, C. Zheng, and B. Shi, *Phys. Rev. E* **65**, 046308 (2002).
  - [24] Y. Guangwu, *J. Comput. Phys.* **161**, 61 (2000).
  - [25] J.-P. Berenger, *IEEE Trans. Antennas Propagat.* **44**, 110 (1996).
  - [26] G.-X. Fan and Q. H. Liu, *IEEE Trans. Antennas Propagat.* **48**, 637 (2000).
  - [27] A. Najafi-Yazdi and L. Mongeau, *Comput. Fluids* **68**, 203 (2012).
  - [28] M. Born, *Z. Phys.* **37**, 863 (1926).